

# Numerical simulation of 3D turbulent boundary layers using the V2F model

By S. Parneix AND P. Durbin

## 1. Motivation and objectives

A 3-D turbulent boundary layer (3DTBL) is usually generated by a change in the geometry, e.g. by a turning channel or an appendage mounted on a channel wall. The resulting spanwise pressure gradient,  $\partial p/\partial z$ , skews the incoming 2-D boundary layer  $U(y)$ , creating an extra strain rate  $\partial W/\partial y$ . The near-wall part of the mean flow, with low momentum, is expected to respond more rapidly to this new pressure gradient than the high momentum free-stream flow. Consequently, variation of the flow turning angle in the normal direction  $y$  is expected.

Experimental databases (e.g. Ölcmen & Simpson 1995, Webster *et al.* 1996) have been used to evaluate the ability of classical linear eddy viscosity models to reproduce a 3DTBL. In all cases, it was observed that a non-zero angle can exist between the direction of the flow gradient and of the shear-stress while, with the isotropic eddy viscosity hypothesis, this angle is exactly zero. This has led to a sentiment that more sophisticated turbulence models (Second Moment Closure, non-linear eddy viscosity) are needed to better predict 3-D ‘complex’ configurations. However, the error associated with prescribing identical directions of Reynolds stress and mean rate of strain may be not crucial in the prediction of the mean flow: at an operational level, the Reynolds stresses are not used, only the eddy-viscosity. In fact, turbulent shear stresses have been found to be smaller than pressure forces in the outer part of the 3-D boundary layer (Johnston & Flack 1996). Moreover, the inner layer of a 3DTBL is a collateral region, i.e. the velocity vectors are coplanar with the wall shear stress direction (Goldberg & Reshotko 1984). If a suitable near-wall turbulence model is being used, these observations give hope that accurate predictions of 3-D turbulent flows can be obtained while keeping the numerically amenable, isotropic eddy viscosity hypothesis.

The *V2F* model was introduced by Durbin (1991) as a restriction of a full Second Moment Closure model (Durbin 1993). It is able to reproduce both the damping of turbulence transport near solid boundaries and the well-known near-wall non-local effects of pressure-deformation fluctuations. Its main advantage is its validity and accuracy up to the wall without using either wall functions or damping functions. This model has been implemented in NASA’s INS3D (Rogers & Kwak 1990) and used herein for computing two 3-D flows. The first is the flow over a swept bump mounted on the floor of a wind tunnel (Webster *et al.* 1996). This case involves both curvature and cross-flow effects. For this case, a new coefficient in the  $\varepsilon$ -model equation, which gets rid of the impractical and ‘ill-behaved’ wall distance, has been compared with the initial version (Durbin 1995) and with the experiment. Then, the model has been directly applied to the more complex, 3-D flow around

a wall-mounted appendage (Devenport & Simpson 1990, Ölcmen & Simpson 1995, Ölcmen & Simpson 1997). This well-documented flow involves a 3DTBL, massive separation, and secondary flow with a horseshoe vortex around the appendage.

## 2. Accomplishments

### 2.1 Flow over a swept bump

#### 2.1.1 Configuration

The experimental configuration is presented in Fig. 1. The bump consists of a short concave section, a longer convex section, and another short concave section. The Reynolds number based on the maximum inlet velocity and the bump chord  $c$  (cf. Fig. 1) is about 323,000. The upstream boundary layer begins at a swept suction slot. It is a fully developed boundary layer with a momentum thickness Reynolds number of 3,800 at one-half chord upstream of the onset of curvature. Since channel side wall effects are negligible in the experiment, the flow is homogeneous in the direction parallel to the line of the bump. This allows a 2-dimensional, 3-component computation to be done. In a frame with the  $\tilde{x}$ -axis perpendicular to the bump and the  $\tilde{z}$ -axis parallel to it, the  $\tilde{z}$ -momentum equation is simply the convection diffusion equation:

$$D_t \tilde{W} = \nabla \cdot \left( (\nu + \nu_t) \nabla \tilde{W} \right) \quad (1)$$

The inlet condition is  $\tilde{W} = U \sin 45^\circ$ ,  $\tilde{U} = U \cos 45^\circ$ . The experimental and computational results are presented in the wind-tunnel  $x - y$  frame. In this frame,  $W$  is equal to 0 at the inlet.

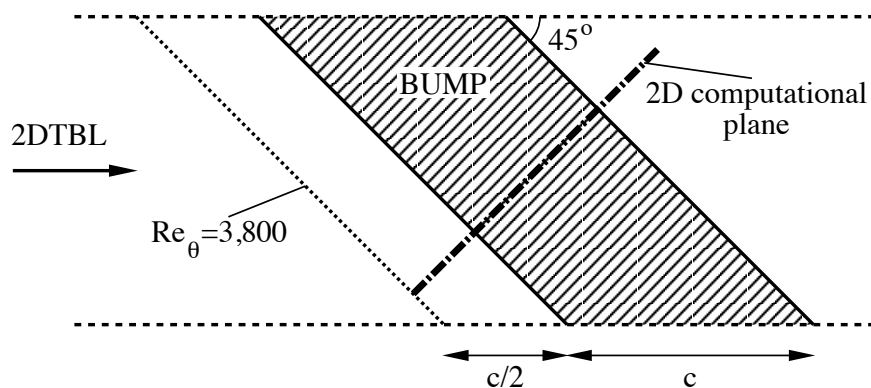


FIGURE 1. Top view of the wall mounted bump.

Inlet profiles of  $k$ ,  $\overline{v^2}$ , and  $\varepsilon$  were obtained from a separate computation of a flat plate boundary layer. The entire channel height is taken into account in all the simulations. These were performed using a general geometry, finite-difference code developed by Rogers & Kwak (1990) to which the  $V2F$  model has been added. The spatial discretization scheme is third-order, upwind biased for convection terms

and second-order, central for diffusion terms. A fine stretched, curvilinear grid of  $150 \times 120$  nodes was used with a high resolution near solid boundaries and around the bump onset and exit. A mesh independency study was performed by dividing the mesh by a factor of 2 in all directions; the results on both mean velocity and skin friction were little changed.

### 2.1.2 Results

Although the minimum distance to the wall,  $d$ , was not used for evaluating the damping of the normal velocity fluctuations at the wall, it was present as an interpolation parameter in Durbin (1995). The motivation was simply to obtain suitable values of  $C'_{\varepsilon_1}$  in the  $\varepsilon$ -equation for both turbulent boundary layers ( $C'_{\varepsilon_1} = 1.55$ ) and plane mixing layers ( $C'_{\varepsilon_1} = 1.3$ ): to this end, the formula  $C'_{\varepsilon_1} = 1.3 + 0.25/[1 + (d/2\ell)^2]^4$  was used. Here  $\ell$  is a turbulent length scale (see Durbin 1995). The distance to the wall is often criticized for being ‘ill-behaved’ in complex, 3-D geometries. It is also impractical to use in multizone computations or in unsteady calculations with moving surfaces. In the present formulation,  $d$  is replaced by the structural parameter  $k/v^2$ , which has similar properties; in particular, it provides a means to increase the production of  $\varepsilon$  near solid boundaries. It does this by the physically attractive route of relating  $C_{\varepsilon_1}$  to the anisotropy of the turbulent velocity fluctuations. The specific formula is  $C'_{\varepsilon_1} = C_{\varepsilon_1}(1 + a_1\sqrt{k/v^2})$ . This is the only change in the equations from those in Durbin (1995). Since this one formula is different, the value of the empirical coefficients had to be recalibrated. For this purpose, the same test-cases as for the initial version were used (a zero-pressure gradient 2DTBL and a low-Reynolds number fully-developed channel flow). The differences between the two versions are indicated below:

- For the initial version (Durbin 1995):  $C'_{\varepsilon_1} = 1.3 + 0.25/[1 + (d/2\ell)^2]^4$

$$C_\mu = 0.19, C_L = 0.3, C_\eta = 70.0 \quad (2)$$

- For the present version:  $C'_{\varepsilon_1} = 1.4(1 + 0.045\sqrt{k/v^2})$

$$C_\mu = 0.22, C_L = 0.25, C_\eta = 85.0 \quad (3)$$

The length scale formula actually involves the product  $C_L C_\eta$ , which is 21 in both (2) and (3). So the recalibration is relatively minor.

These two versions have been compared on the configuration of the swept bump. The pressure and friction coefficients (Figs. 2 and 3) as well as mean flow profiles (not shown here) obtained by both versions are very similar to each other. It should be added that the new version, i.e. with  $k/v^2$ , has been checked to give similar results, without affecting the numerical stability, in most of the previous two-dimensional test-cases performed with the first version, including adverse pressure gradient boundary layers and recirculating or impinging flows. The two formulas for  $C'_{\varepsilon_1}$ , having very similar behaviors, are viable alternatives. The present formulation

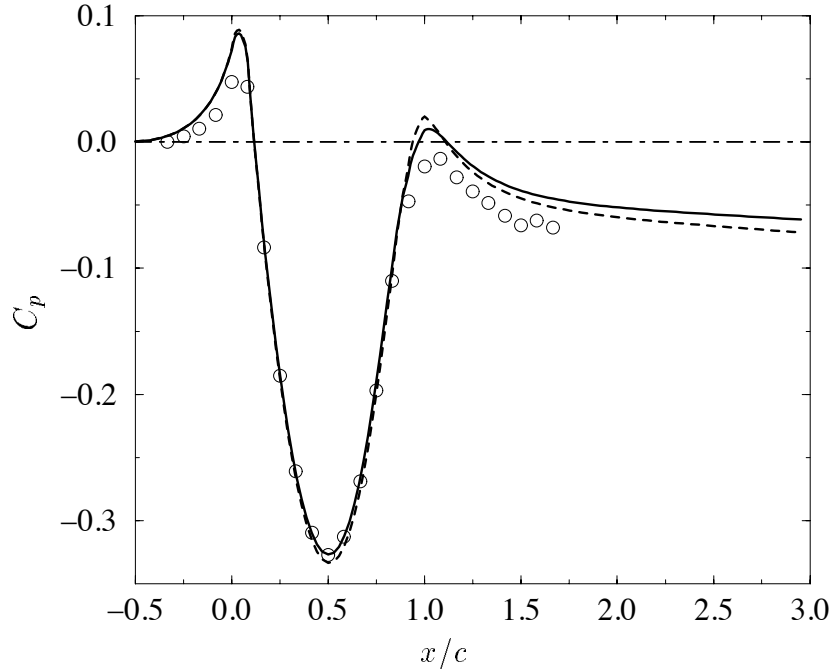


FIGURE 2. Pressure coefficient, — :  $V2F$  with  $d$  (Durbin 1995), ---- :  $V2F$  without any reference to  $d$ ,  $\circ$  : Webster *et al.* experiment (1996).

has the advantage of not involving the distance to the wall, which may be crucial in 3-D multizone complex configurations.

The results of the  $V2F$  model are now compared with the Webster *et al.* experiment (1996). The discussion will be valid for both versions. For all the following figures,  $x$  is taken as the streamwise axis of the wind tunnel,  $y$  is the normal axis,  $z$  will be the spanwise axis, across the wind tunnel. The homogeneous direction is  $45^\circ$  to the  $x$ -axis. All the profiles will be presented with length normalized by  $c$ , the chord of the bump in the wind-tunnel cross sectional plane. The scaled height of the wind tunnel is then  $1/2$ . The origin of the  $x$ -axis is at the onset of the bump, so the bump ends at  $x = 1$ .

Figure 2 shows the pressure coefficient along the wall. The presence of the bump first creates a mild adverse streamwise pressure gradient upstream. At the onset of the bump, the regime becomes a strong favorable pressure gradient. The rear of the bump is a region of strong adverse pressure gradient, and the boundary layer recovers in a zero pressure gradient, after a mild favorable pressure gradient region, downstream. One can see that the  $V2F$  model reproduces these trends quite well, both qualitatively and quantitatively. Perhaps the downstream recovery is a bit less rapid than in the experiment.

The bump is low enough that separation does not occur in its lee side. This made the maintenance of an infinitely swept condition easier in the experiment. The  $V2F$  predictions of the spanwise skin friction coefficient, which characterizes the three-dimensionality of the flow, are in excellent agreement with the experimental data (see Fig. 3). As indicated above, the flow is skewed several times by the spanwise

pressure gradient. The changes in sign of the spanwise friction coefficient,  $C_f^z$ , are accurately reproduced by the  $V2F$  model. The most notable discrepancy is in the level of the streamwise skin friction coefficient,  $C_f^x$ , over the bump. This problem also appears in the 2-D case (Wu & Squires 1997a), so it is not related to the three-dimensionality of the flow. There is a possibility that the flow is close to relaminarizing due to the strong favorable pressure gradient on the windward side of the bump.

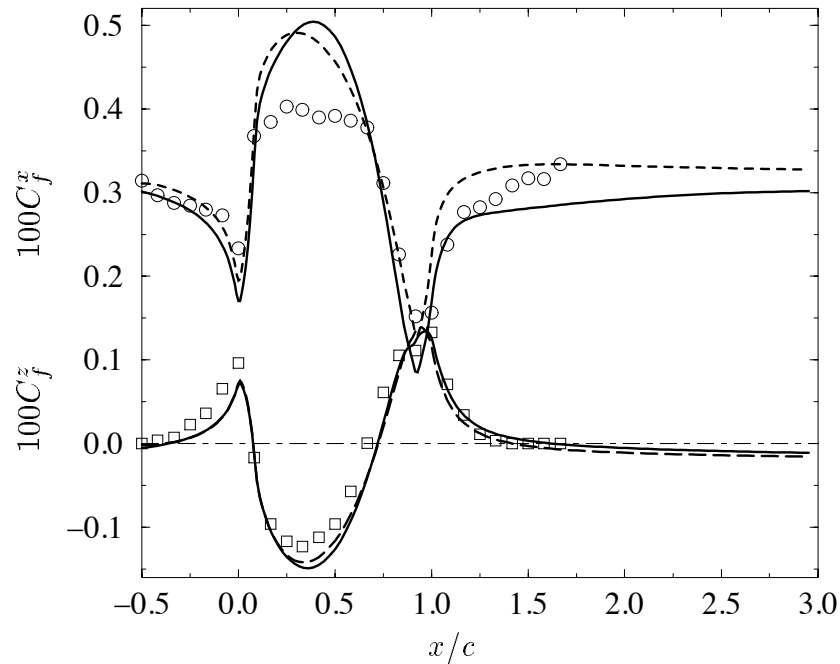


FIGURE 3. Streamwise and spanwise friction coefficient, — :  $V2F$  with  $d$  (Durbin 1995); ---- :  $V2F$  without any reference to  $d$ ;  $\circ$  :  $100C_f^x$ , Webster *et al.* experiment (1996);  $\square$  :  $100C_f^z$ , Webster *et al.* experiment (1996).

## 2.2 Flow around an appendage-body junction

### 2.2.1 Configuration

Since both versions of the  $V2F$  model gave very similar results, the computations presented in this section were done only with the present one, which gets rid of the distance to the wall. The studied configuration concerns the turbulent flow around an appendage mounted on a flat plate. The obstacle consists of a 3:2 elliptical nose and a NACA 0020 tail joined at the maximum thickness  $t$  (Fig. 4). There are neither sweep nor incidence angles; the flow is symmetric and only half of the domain was actually computed. The incoming boundary layer was tripped in the experiment so that inlet conditions are clean and well defined: at 0.75 chord upstream of the nose, the zero pressure gradient 2DTBL has a momentum thickness Reynolds number of  $Re_\theta = 5,940$ . The Reynolds number based on the chord length  $c$  of the obstacle and the maximum velocity of the incoming 2DTBL,  $U_0$ , is about  $4.4 \times 10^5$ . The experimental database used for comparisons consists of a set of

several well documented experiments conducted at Virginia Polytechnic Institute (Devenport & Simpson 1990, Ölcmen & Simpson 1995, Ölcmen & Simpson 1997). This test-case is much more complicated than the swept bump since a fully 3-D computation is required. The presence of the appendage does create a 3DTBL, but other complex phenomena such as curvature of the obstacle, 3-D separation, and a horseshoe vortex are also involved. Indeed, the lower wall boundary layer is both skewed by the presence of the obstacle and also experiences an adverse pressure gradient in front of the nose of the obstacle that causes the flow to separate upstream of the leading edge. A recirculation is created in the symmetry plane. This vortical structure is stretched around the junction, and its direction is reoriented along the appendage. Although the geometry is fairly simple, the flow is very complex and is a challenging test-case for turbulence models. Note that accurate predictions of the horseshoe vortex may be of industrial importance, e.g. heat transfer is strongly enhanced by the presence of this kind of secondary flow structure [Spencer *et al.* 1996, Praisner *et al.* 1997].

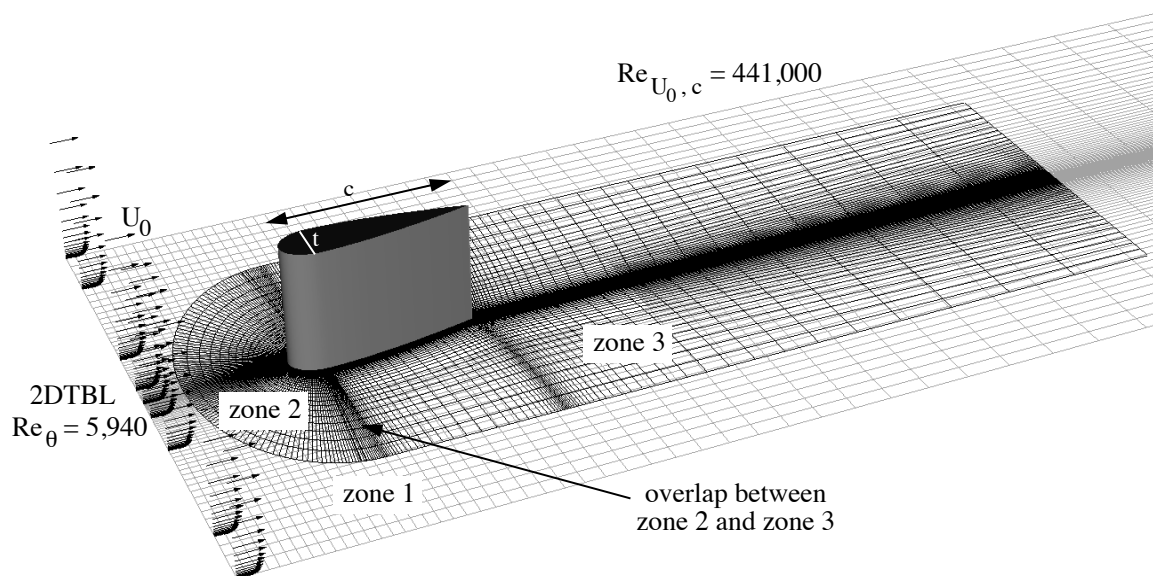


FIGURE 4. The geometry and flow conditions of the turbulent flow around a wall-mounted appendage.

A multizone grid was used with a high resolution near solid boundaries; basically, the distance between any boundary node and the closest computational point was less than  $y^+ = 5$  in wall units. This assures an accurate resolution of the viscous layer. The first zone is gridding the experimental channel: it is Cartesian and allows imposition of the right spanwise blockage ratio and inlet conditions. In the experiment, inserts for the wind-tunnel side-walls were constructed to minimize blockage-induced pressure gradients around the obstacle (Devenport & Simpson 1990): these are not modeled in our computations, instead slip conditions have been imposed. The influence of these boundary conditions has been checked to

be negligible by increasing the channel width by a factor of 2 without any major modification of the results. The two other zones are curvilinear and adapt to the obstacle. The first (zone 2) is restricted to the nose, where separation and the horseshoe vortex arise; the second (zone 3) is discretizing the tail and the wake. The link between each zone is performed by Chimera interpolation stencils (Benek *et al.* 1985, Benek *et al.* 1987). This technique has been applied with success for a long time to CFD. It is considered to be very efficient if there are no sharp gradients normal to the inter-zonal boundaries — which is the case in our computations. The results presented in this section have been performed with a three-zone grid of 210,000, 231,000, and 231,000 nodes, respectively: i.e., 672,000 discretization points in total.

### 2.2.2 Results

Figure 5 shows a comparison between an oil-flow visualization performed on the experimental test wall by Ölcmen & Simpson (1995) and a set of wall-streamlines from the computation (trajectories of particles released at the first computational point above the flat plate). A line of separation wrapped around the obstacle shows the position of the horseshoe vortex, denoted ‘H’. One sees good qualitative agreement between the  $V2F$  model and experiment. Predictions of the location and the extent of the separation line are very similar to the oil-flow visualizations. The wake seems also to be well estimated. The experiment shows evidence of the existence of a recirculation near the trailing edge, denoted ‘T’, also predicted by the  $V2F$  simulation. No specific data are available for this latter phenomenon. Nevertheless, a large database will be used for quantitative comparisons; it concerns the development of the 3DTBL outside of the separation line (stations 1 to 7 in Fig. 5), the recirculation in the symmetry plane upstream of the appendage’s leading edge (measurement points are indicated on the figure), and the horseshoe vortex secondary flow (with measurements in the plane perpendicular to the flat plate and to the obstacle, passing through station 5).

Since the simulation of a 3DTBL was the first topic of this study, some comparisons of the spanwise velocity profiles measured at several locations (stations 1 to 7, see Fig. 5) outside of the separation line are presented in Fig. 6. These locations correspond to LDV and hot-wire experimental measurements (Ölcmen & Simpson 1995). Note that the  $y$ -axis is in a logarithmic scale; this exaggerates the near-wall region. As expected, the most important effect of the spanwise pressure-gradient is seen close to the wall. The maximum amount of cross-flow increases continuously until stations 4 and 5 (up to 20% of the reference velocity  $U_0$ ) and then decreases again. The location of these maxima shifts to a higher  $y$ -location at each successive location. The agreement between the  $V2F$  model and the experiment is excellent both qualitatively and quantitatively. This computation confirms the results obtained for the swept bump, where the 3DTBL is very well represented by the simulations, even though the linear eddy viscosity hypothesis is being used.

Devenport and Simpson (1990) reported some LDV measurements in the symmetry plane upstream of the nose of the appendage. They characterized the action of the adverse pressure-gradient on the flow with a separation and a recirculation

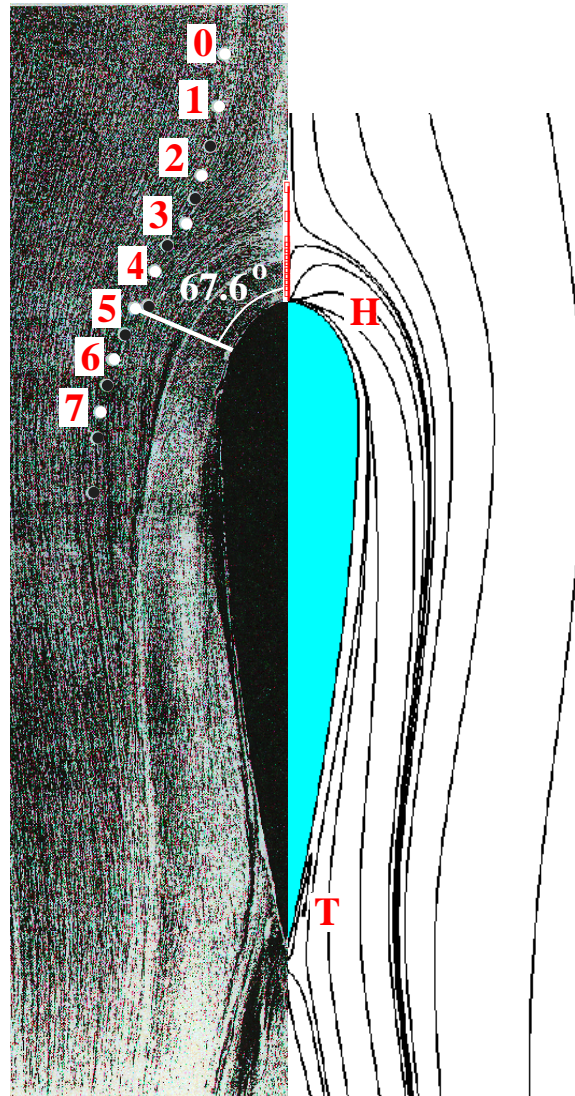


FIGURE 5. Ölcmen & Simpson (1995) experimental oil-flow visualization (on the left) and computational wall-streamlines (on the right).

bubble. They noted the existence of bimodal histograms of velocity fluctuations, associated with very-low frequencies. This kind of feature is radically different from vortex-shedding and cannot be represented by a RANS calculation. Nevertheless, the frequency of this large-scale unsteadiness is much lower than the passage frequency of coherent structures, which may suggest that only a small fraction of the turbulent structures will be influenced by this bimodality. Figure 7 shows the  $U$ -profiles in the symmetry plane in front of the obstacle. The experimental streamwise velocity indicates the separation location around  $x/t = -0.35$ . The  $V2F$  computation shows that the flow has just separated at  $x/t = -0.35$ . Profiles at  $x/t = -0.40$  and  $-0.30$  are well-established unseparated and backflow profiles, respectively, which indicates a separation location close to  $-0.35$ , in excellent

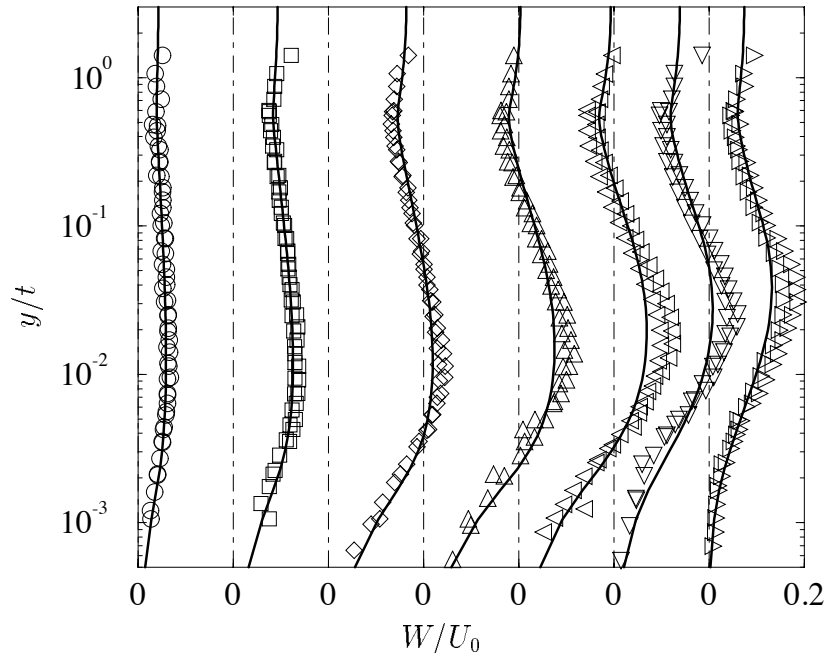


FIGURE 6. Spanwise velocity profiles of the 3DTBL, symbols: Ölcmen & Simpson experiment (1995) for stations 1 ( $\circ$ ), 2 ( $\square$ ), 3 ( $\diamond$ ), 4 ( $\triangle$ ), 5 ( $\triangleleft$ ), 6 ( $\nabla$ ) and 7 ( $\triangleright$ ), — :  $V2F$  model.

agreement with the experiment. The intensity of the backflow is basically well reproduced, even if it is slightly under-predicted in the middle of the recirculation (40% of the nominal velocity instead of 50%). Moreover, in the bubble the extension of the backflow, normal to the plate, seems to be a little more spread out in the experiment. Note also that the model is able to reproduce a kink of  $U$ , present at the end of the log-region (around  $y/t \simeq 0.5$ ) in the profiles between  $x/t = -0.35$  and  $-0.20$ .

Figure 8 shows contours of the turbulent kinetic energy,  $k$ , in the symmetry plane. One can observe a strong similarity between the experiment and the  $V2F$  simulation. As it has been pointed out by Behnia *et al.* (1997), the  $V2F$  model is able to predict the right damping of turbulent transport near the wall, especially in the impinging region. In this area (along the wing in the symmetry plane), all  $k - \varepsilon$  computations reported in the 4th ERCOFTAC/IAHR workshop on refined flow modeling (1995) show a large, spurious production of turbulence, in total disagreement with the experiment. One can also see that the location, shape, and size of the region where high levels of turbulence exist is very well reproduced by the  $V2F$  model. This is a notable improvement over the  $k - \varepsilon$  simulations. Quantitatively, the maxima measured levels of  $k$  are about 30% higher than those predicted by the computation (see Fig. 8). A good agreement is obtained outside of the recirculation zone (both for the 2-D adverse pressure-gradient flow and in the vicinity of the appendage), but a strong under-prediction does exist inside the vortex. Devenport & Simpson (1990) noticed that high values of production of  $k$  are present in the region where the flow is bimodal (basically in the middle of the recirculation) and concluded that this strong

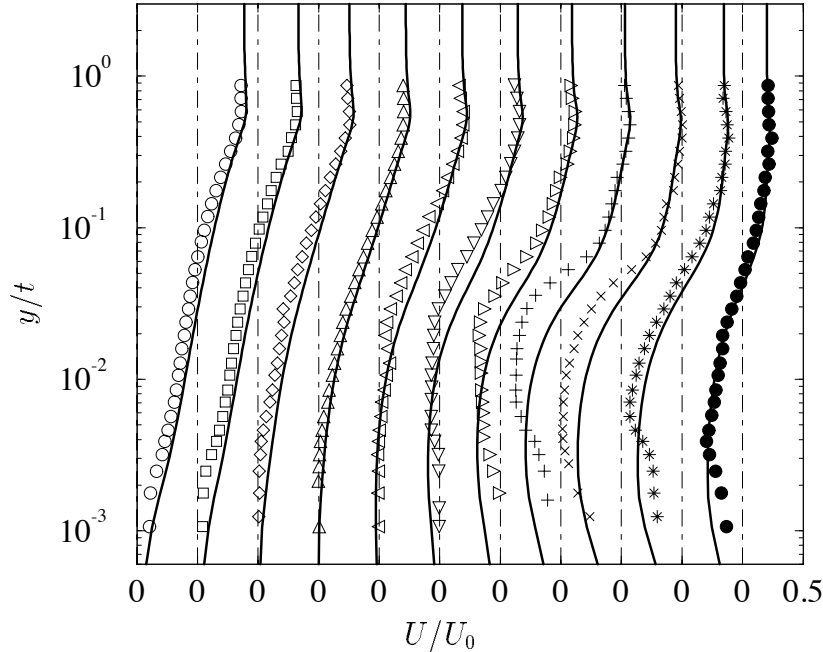


FIGURE 7. Streamwise velocity profiles in the symmetry plane upstream of the appendage's nose, symbols: Devenport & Simpson experiment (1990), for  $x/t = -0.86$  ( $\circ$ ),  $-0.65$  ( $\square$ ),  $-0.46$  ( $\diamond$ ),  $-0.40$  ( $\triangle$ ),  $-0.35$  ( $\triangleleft$ ),  $-0.30$  ( $\nabla$ ),  $-0.25$  ( $\triangleleft$ ),  $-0.20$  ( $+$ ),  $-0.15$  ( $\times$ ),  $-0.10$  ( $*$ ),  $-0.05$  ( $\bullet$ ), — :  $V2F$  model.

turbulence production was a result of stochastic large-scale unsteadiness rather than conventional shear layer-mechanisms. Based on the present computational results, we may conclude that turbulent quantities seem to be affected by this bistable feature, which cannot be captured by any Reynolds-average turbulence model, but the influence on the mean flow is rather small.

Since the intensity and location of the base of the horseshoe vortex is well predicted (in the symmetry plane), it is interesting to see whether the model is able to reproduce the development around the appendage of the secondary flow associated with this structure. Ölcmen & Simpson (1997) recently reported some flow measurements in a plane normal to the obstacle and the surface. This plane passes through station 5 (see Fig. 5). In this plane, the horseshoe vortex has already turned an angle of  $67.6^\circ$  around the appendage.

Secondary flow streamlines are presented in the background of Fig. 9. These represent particles trajectories in the measurement plane. In this figure, the reference frame has changed:  $y$  is still the coordinate normal to the flat plate and  $s$  is the coordinate in the plane, normal to the obstacle, denoted as the radial coordinate. Positive values of the flow angle point in the inward direction. A log-scale has been used to focus on the near wall flow and to see the real accuracy of the predictions. The horseshoe vortex is clearly present. A large rotational region shapes the structure of the whole appendage-body junction flow. In this plane, the vortex center is located at about  $\log_{10}(y/t) \simeq -1.1$  and  $s/t \simeq 0.32$  in the experiment.

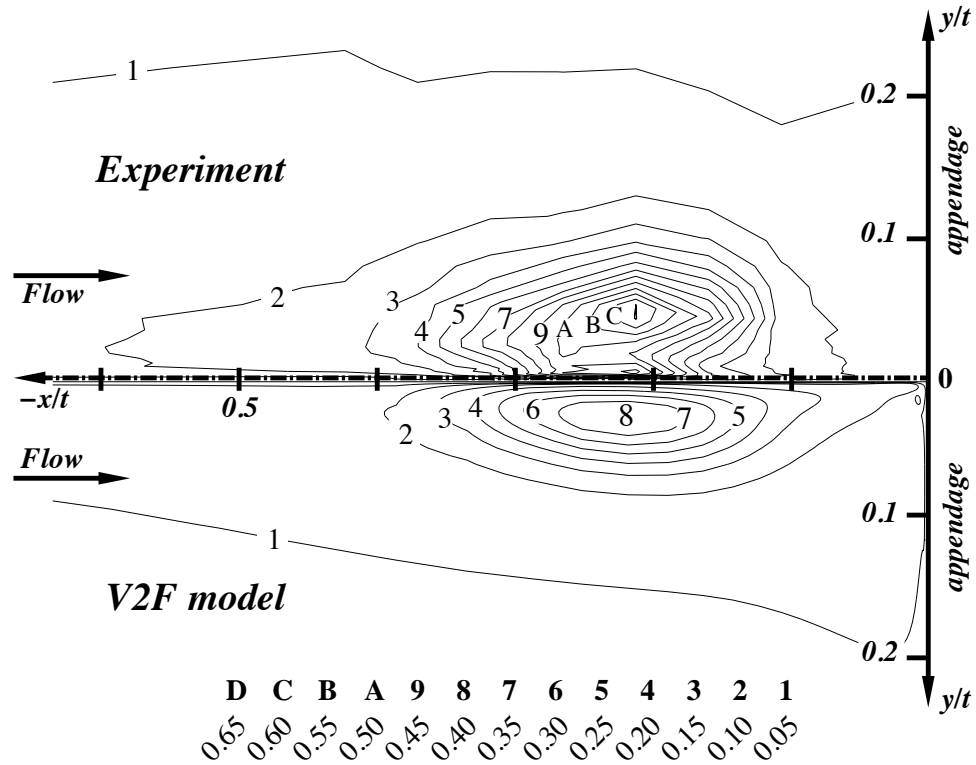


FIGURE 8. 2D-contours of turbulent kinetic energy in the symmetry plane upstream of the appendage's nose.

The simulated secondary flow shows strong similarities with the experiment. The free-stream fluid is directed towards the appendage and rolls around the center of the vortex. Its location is predicted at  $\log_{10}(y/t) \simeq 1.1$  and  $s/t \simeq 0.28$ . One can observe a line of 0 radial velocity with outward flow on one side and inward flow on the other side. The location of this line at the lower wall shows the location of the 3-D separation line seen in Fig. 5. At  $y/t \simeq 10^{-3}$ , which is very close to the wall, the model is in excellent agreement with the experiment, showing a separation line location of about  $s/t \simeq 0.5$ . The *V2F* computations predict a tiny, secondary, counter-rotating structure very close to the appendage that is also present in the experiment. Figure 9 also shows contours of the flow angle, relative to the measurement plane, computed as  $\arctan(W/U)$ ,  $U$  being the tangential velocity component (normal to the measurement plane) and  $W$  being the radial velocity component (normal to the obstacle). The flow is deflected up to  $12^\circ$  towards the appendage and up to  $24^\circ$  away from it. Even if the levels are slightly under-estimated, one can see that the model is able to predict successfully the whole qualitative and quantitative distribution of the turning angle in this cutting plane.

### 3. Conclusion

A modification of the  $\varepsilon$  model equation, which allows the *V2F* model to be free of any reference to the distance to the wall, has been presented. The modification

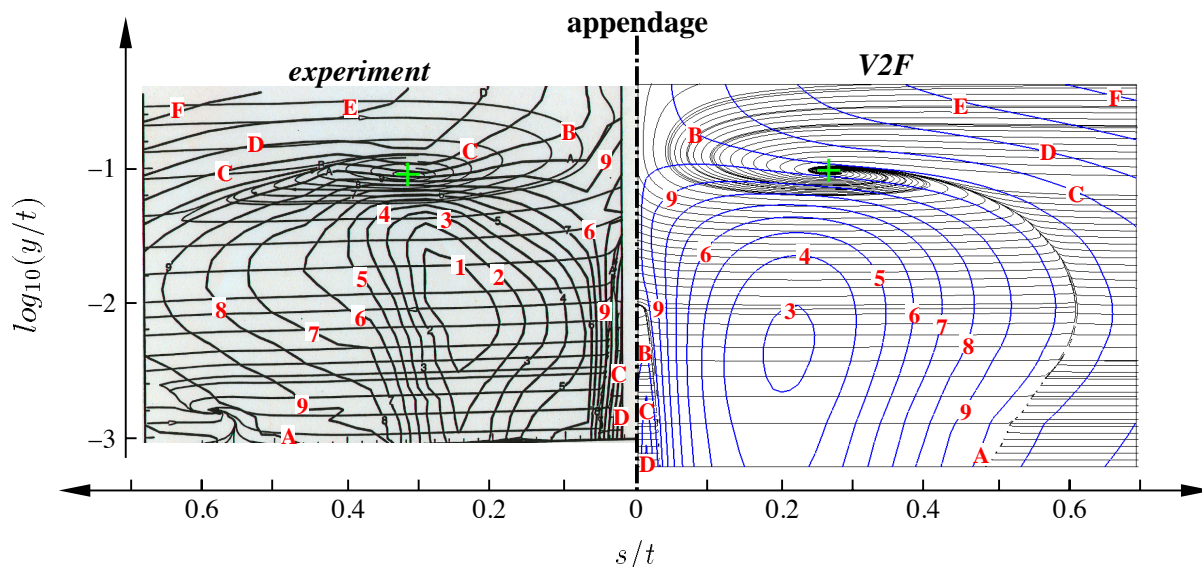


FIGURE 9. Flow angle— $\arctan(W/U)$ —contours and secondary streamlines in background, in the plane normal to the obstacle and to the surface passing through station 5 (see Fig. 5); levels of flow angle:  $-24.1^\circ$  (1),  $-21.6^\circ$  (2),  $-19.0^\circ$  (3),  $-16.4^\circ$  (4),  $-13.9^\circ$  (5),  $-11.3^\circ$  (6),  $-8.7^\circ$  (7),  $-6.1^\circ$  (8),  $-3.5^\circ$  (9),  $-1.0^\circ$  (A),  $1.6^\circ$  (B),  $4.2^\circ$  (C),  $6.7^\circ$  (D),  $9.3^\circ$  (E),  $11.9^\circ$  (F).

makes use of the measure of anisotropy,  $\overline{v^2}/k$ , provided by the model. This version gives very similar results (in terms of accuracy and stability) to the original one, but it is more suitable for computations in 3-D, complex, multizone configurations.

After the implementation of the *V2F* model in NASA's CFD code, INS3D, computations of three-dimensional turbulent boundary layers have been performed. Despite the linear eddy viscosity hypothesis, the model is able to reproduce the main features of the mean quantities. The secondary flow and the turning angle are predicted correctly both qualitatively and quantitatively in both cases of a swept bump and an appendage mounted on a flat plate. The latter presents a fairly complex 3-D flow including separation and a horseshoe vortex. It is a challenging test-case for turbulence models; *V2F* computations agree very well with the experiment. The description of the horseshoe vortex is reproduced accurately in terms of its location and intensity, even if the secondary flow is slightly under-estimated. The position of the 3-D separation line is correctly simulated and a counter-rotating horseshoe vortex has even been found close to the appendage-body corner, in agreement with the experiment.

In the future, the *V2F* model needs to be applied to flows getting closer to the configurations met in industry. In particular, we plan to study the effects of rotation, heat transfer, or compressibility associated with some more 3-D complex geometries.

#### REFERENCES

- BEHNIA, M., PARNEIX, S. & DURBIN, P., 1997 Accurate predictions of jet impingement heat transfer. *HTD-Vol. 343 Nat. Heat Transfer Conf., Book No*

- H0190*. **5**, 111-118.
- BENEK, J.A., BUNNING, P.G. & STEGER, P.G., 1985 Chimera: a gridembedding technique. *AIAA paper No. 85-1523*.
- BENEK, J.A., DONEGAN, T.L. & SUHS, J.L., 1987 Extended Chimera grid-embedding scheme with applications to viscous flows. *AIAA paper No. 87-1126*.
- CHEN, H.C., 1995 Assessment of a Reynolds stress closure model for appendage-hull junction flows. *J. of Fluid Eng.* **117**, 557-563.
- DEVENPORT, W. & SIMPSON, R., 1990 Time-dependent and time-averaged turbulence structure near the nose of a wing-body junction. *J. of Fluid Mech.* **210**, 23-55.
- DURBIN, P., 1991 Near-wall turbulence closure modeling without "damping functions". *Theoret. Comput. Fluid Dynamics*. **3**, 1-13.
- DURBIN, P., 1993 A Reynolds-stress model for near-wall turbulence. *J. of Fluid Mech.* **249**, 465-498.
- DURBIN, P., 1995 Separated flow computations with the  $k - \varepsilon - \overline{v^2}$  model. *AIAA Journal*. **33 No.4**, 659-664.
- ERCOFTAC/IAHR, 1995 4th ERCOFTAC/IAHR Workshop on refined flow modeling.
- GOLDBERG, U. & RESHOTKO, E., 1984 Scaling and modeling of three-dimensional, pressure-driven turbulent boundary layers. *AIAA Journal*. **22**, 914-920.
- JOHNSTON, J.P. & FLACK, K.A., 1996 Review - Advances in three-dimensional turbulent boundary layers with emphasis on the wall-layer regions. *J. of Fluid Eng.* **118**, 219-232.
- MOIN, P., SHIH, T.H., DRIVER, D.M & MANSOUR, N.M., 1995 Direct numerical simulation of a three-dimensional turbulent boundary layer. *Physics of Fluids A*. **2**, 601-639.
- OLCMEN, S. & SIMPSON, R., 1995 An experimental study of a three-dimensional pressure-driven turbulent boundary layer. *J. of Fluid Mech.* **290**, 225-262.
- OLCMEN, S. & SIMPSON, R., 1997 Some features of a turbulent wing-body junction vortical flow. *AIAA paper No. 97-0651*.
- PRAISNER, T.J., SEAL, C.V., TAKMAZ, L. & SMITH, C.R., 1997 Spatial-temporal turbulent flow-field and heat transfer behavior in end-wall junctions. *Int. J. of Heat and Fluid Flow*. **18**, 142-151.
- ROGERS, S. E. & KWAK, D., 1990 Upwind differencing scheme for the time-accurate incompressible Navier-Stokes equations. *AIAA Journal*. **28**, 253-262.
- SPENCER, M.C., JONES, T.V. & LOCK, G.D., 1996 Endwall heat transfer measurements in an annular cascade of nozzle guide vanes at engine representative Reynolds and Mach numbers. *Int. J. of Heat and Fluid Flow*. **17**, 139-147.
- SUNG, C.H. & YANG, C.I., 1988 Validation of turbulent horseshoe vortex flows. *17th Symposium on Naval Hydrodynamics, La Hague*.

- WEBSTER, D.R., DEGRAAFF, D.B. & EATON, J.K., 1996 Turbulence characteristics of a boundary layer over a swept bump. *J. of Fluid Mech.* **1996**, 323, 1-22.
- WU, X. & SQUIRES, K.D., 1997a Nonequilibrium turbulent flow over a bump: a comparison of LES and RANS with experiments. *Submitted to AIAA Journal*.
- WU, X. & SQUIRES, K.D., 1997b Prediction of the three-dimensional turbulent boundary layer over a swept bump. *Submitted to AIAA Journal*.